

# Waverider Design, Analysis and Performance Evaluation

Frederick Ferguson<sup>1</sup>, Mookesh Dhanasar<sup>2</sup>, Nastassja Dasque<sup>3</sup>, and Chuka Onuorah<sup>4</sup>  
*Mechanical Engineering Department, NCAT, Greensboro, NC 27411, USA*

Isaiah M. Blankson<sup>5</sup>

*NASA Glenn Research Center, Cleveland, OH, USA*

This paper discusses the development and validation of a suite of tools, having both geometric and performance based characteristics, that when used in concert generate waverider configurations with realistic flying capability. The geometric tools incorporate an algorithmic coupling to the directional derivatives of the fluid dynamic conservation laws to produce flow fields in the form of organized sets of post-shock wave stream-surfaces. From these stream-surfaces, waverider configurations are constructed. These performance based routines were created with the goals of efficiently and accurately evaluating the aerothermo-dynamic performance of the resulting hypersonic configurations. In efforts to continuously improve the efficiency of the waverider toolset, the numerical procedures, with capability of evaluating the local pressure, skin-friction and heat flux distribution on the hypersonic configurations, are constantly improved and validated. For example, the performance parameter tools, in regions where the surfaces of vehicle configuration allow for the use of planar models. In regions, such as, the blunted leading edges, the modified Newtonian theory, Fay-Riddell theory and Modified Reynolds analogy are applied. In general, the waverider design and evaluation code consist of a suite of elementary design algorithms that are either based on existing analytical solutions, empirical relationships, or independent computer simulation. For example, a set of streamlines that is generated from an arbitrary shockwave can also be quickly be compared to the equivalent set of streamlines generated for the exact Taylor-Maccoll solution. In a similar manner, the observed relationships between the local Stanton number and skin friction coefficient with local Reynolds number along the idealized region of the vehicle surface can quickly be compared to that of experimental findings.

Of particular importance this study, is the creation of an automated grid generation tool. For the purposes of independent CFD simulations, structured mesh, orthogonal to both the hypersonic vehicle surface and the free stream, can be generated around the resulting hypersonic vehicle configuration. Additionally, as per the user's requirements, the grid information can be exported to appropriate CFD codes in their respective format. The independent CFD simulations compared well with the data predicted by the suite of hypersonic vehicle design tools. For example, when comparing the external flow fields generated by independent CFD simulations tools to that of the hypersonic vehicle design tool, it can be observed that all the main features are recovered. In the case of conical flow fields, the exact Taylor-Maccoll solution is recovered. Additionally, in all cases, the pressure distribution on the vehicle surface compares extremely well to that from independent analysis. However, the distribution of the viscous-related surface properties generated by the two methods, the independent CFD simulations and the vehicle suite of design tools, occasionally showed some disagreements in the neighborhoods of the blunted edges. These results indicate that there may be room for improvements in the aerothermo-dynamic capability of the hypersonic design code.

## I. Waverider Development Efforts

Waveriders, as presented in Figures 1 and 2, are defined as idealized hypersonic vehicle configurations that are carved from inviscid stream surfaces. Common properties to all waveriders are; (a) the attached shockwaves along their entire leading edges that traps the high pressure flow below their lower surfaces, (b) the ability to permit undisturbed freestream flow above their upper surfaces, and (c) the ability to prevent significant flow leakage from their lower to upper flow fields. In the late nineteen fifties, to meet the waveriders hypersonic vehicle design challenges Terrence Nonweiler proposed an inverse design 'waverider' methodology<sup>4</sup>. In flight, Nonweiler's configurations appears to be

<sup>1</sup> Professor, Mechanical Engineering Department, NCAT and AIAA Associate Fellow.

<sup>2</sup> Research Associate Scholar, Mechanical Engineering Department, NCAT, and AIAA Senior Member.

<sup>3</sup> Post Doctoral Scholar, Mechanical Engineering Department, NCAT, and AIAA Student Member.

<sup>4</sup> MS. Student, Mechanical Engineering Department, NCAT, and AIAA Student Member.

<sup>5</sup> Senior Technologist, NASA Glenn Research Center and AIAA Associate Fellow.

riding the shock wave they generate. At the time of its proposal, Nonweiler's waverider design concept solved a major re-entry problem. It provided the framework for a class of re-entry vehicle configurations with the much needed high 'lift-to-drag' ratios, (L/D), desperately sought by designers. High 'lift-to-drag' ratios provide the control authority needed for long range glided reentry landings. Nonweiler's waveriders were constructed primarily from planar shock waves, resulting in the generation of configurations with extremely sharp leading edges and a distinct 'caret' shape, refer to Figure 1. As can be observed in Figures 1 and 2, Nonweiler's 'caret' waveriders presented 'volumetric' efficiencies and severe 'aerothermo-dynamic leading edge' problems that rendered them unrealistic.

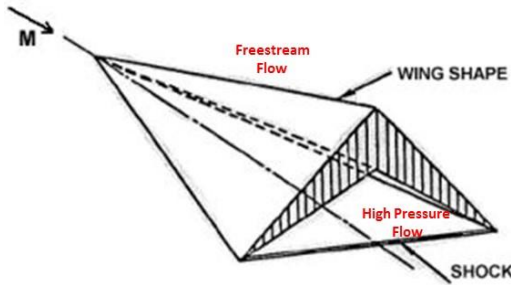


**Fig. 1:** Waverider derived from a planar shock wave<sup>1</sup>

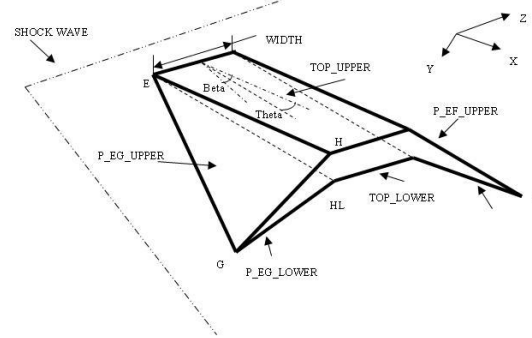


**Fig. 2:** Waverider derived from a planar shock wave<sup>1</sup>

### A: Hypersonic Vehicle Design Requirements

There are many on-going research efforts geared towards the realization of hypersonic flight, Ref. 1-5. Results and lessons learned from research programs conducted in the early 1980s by NASA are presented in Figures 3 - 5, Ref. 1-2. The NASA generic hypersonic transport vehicle configuration was subjected to a series of wind-tunnel tests, and demonstrated that it was not capable of achieving wind-tunnel speeds up to Mach 8. Examination of the wind tunnel data revealed that the NASA generic hypersonic transport vehicle configuration performance parameter; the Lift-over-Drag, L/D, decreased significantly with increasing Mach number. This performance parameter; the Lift-over-Drag, L/D, versus the Mach number, M, phenomenon was extensively investigated by Kuchemann, Ref. 5. Kuchemann conducted a broad scope and detailed study of human flight vehicles, where the aerodynamic performance, L/D along with the vehicles' shape as a function their flight Mach numbers were observed. The major conclusions from Kuchemann's studies are presented in Figures 4 and 5. Figure 4<sup>4-6</sup> illustrates a plot of the maximum aerodynamic performance, L/D, versus the flight Mach number based on data obtained during flight tests and during experimental studies. Also, in Figure 4<sup>5-7</sup>, the open circles represent experimental data obtained from conventional hypersonic vehicles. The solid line represents an empirical relationship between vehicle flight performance, L/D, and Mach number, M, as formulated by Kuchemann<sup>5</sup>. First, Kuchemann identified a 'L/D barrier', as represented by the broken line in Figure 4. Kuchemann concluded that aircraft configurations perform best below this barrier, and in general are not expected to break it. Second, as presented in Figure 5, Kuchemann observed that at high Mach numbers, aircraft with features, such as; blended body configurations with tightly integrated fore-bodies, propulsion and nozzle after-bodies are favored<sup>5</sup>.

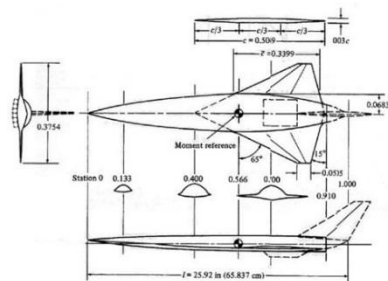


**Fig. 3:** NASA Hypersonic Vehicle<sup>2</sup>

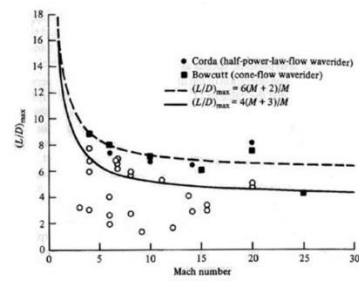


**Fig. 4:** Kuchemann's L/D barrier<sup>4-6</sup>

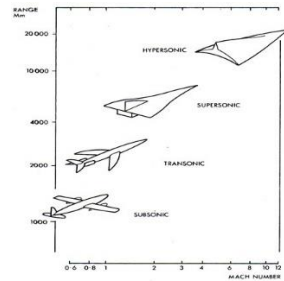


**Fig. 5:** Mach versus aircraft shape<sup>4-6</sup>

## B: Viscous Optimized Waveriders

Studies which take into account the real world effects on waveriders gives rise to the term ‘viscous waveriders’. During the mid-eighties a series of studies on waveriders derived from conical flow fields, that included the viscous effects, was conducted by Kevin Bowcutt<sup>6</sup>. He evaluated their aerodynamic performance as a function of Mach number and demonstrated that this new class of waveriders, nicknamed, the ‘viscous optimized’ waveriders, were capable of breaking the ‘Kuchemann L/D barrier’. In fact, Bowcutt<sup>6</sup> established a new barrier which is presented by the ‘broken line in Figure 4. Bowcutt’s findings were later reinforced by Corda et al and others, see for example Refs. 6 – 12. Both Bowcutt’s and Corda’s waveriders<sup>6-8</sup> L/D performance data are presented in Figure 4.

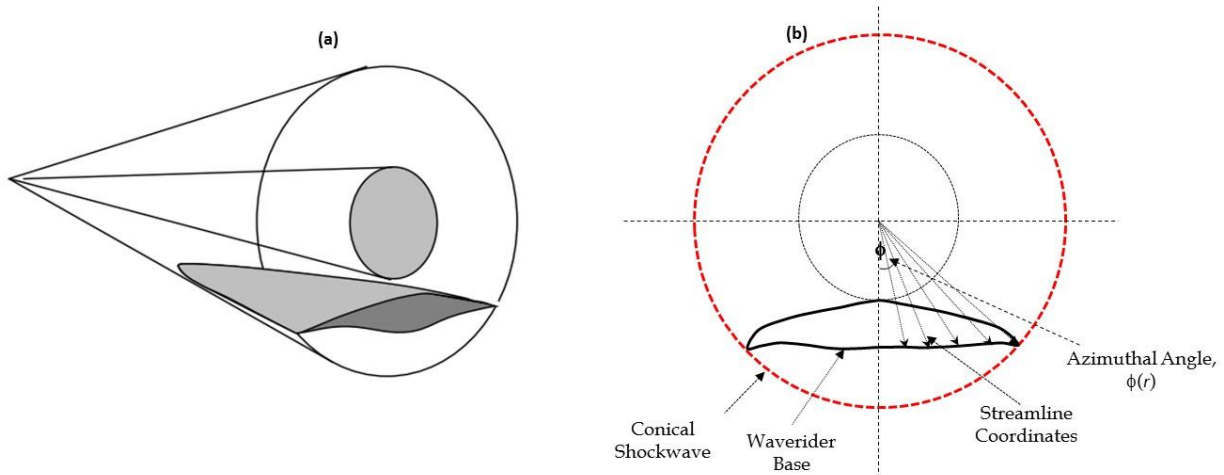


**Fig. 6:** Waverider derived from Conical flowfield<sup>12, 21</sup>

During the derivation of the ‘viscous optimized waveriders’, Bowcutt used the Taylor-Maccoll numerical technique to solve the inviscid supersonic flow between a prescribed conical shock wave and its generating cone<sup>6, 8</sup>. As presented in Figure 6<sup>12, 21</sup>, the upper and lower surfaces of the waverider are defined by prescribing a leading edge curve on the prescribed shock wave, while upper and lower stream lines are traced from every point of the prescribed leading edge curve. The upper surface of the body was designed by assuming it is a freestream surface, while the lower surface were derived from streamlines that follow the behavior of the conical flow field. The result of this design process is a three-dimensional configuration riding an inviscid supersonic flow with its leading edge attached to the shock wave.

## II. Waverider Design Methodology

In this paper, a waverider is defined as an aerodynamic configuration inversely created from a prescribed hypersonic flow field. The hypersonic flow fields can be prescribed by either planar or conical shock waves from which the aerodynamic configuration is carved via streamlines emanating from the shock surface, as presented in Figure 6. When constructed correctly, waveriders are expected to possess superior aerodynamic performance characteristics as they perfectly recreate the flowfields from which they are carved. However, constructing viscous optimized waveriders, as those illustrated in Figure 6, is not a simple task, as many aerodynamics designers, have confirmed.

In an effort to meet this challenge, and to capture the complexity of the real-world flowfield physics, this paper describes a design methodology capable of generating viscous optimized waveriders. A suite of ‘waverider’ derived computational tool, based on the design methodology, is created in an object-oriented Fortran90 format. Essentially, the suite of ‘waverider’ derived computational tool can be organized into two broad categories; (i) the ‘geometric carving’ tools, and (ii) the ‘configuration performance evaluation’ tools. The following sections, A – E, provide brief descriptions of the processes and associated physics used in the development of these tools.

### A. Creating Inviscid Flow fields from Prescribed Shock Waves

Every design process requires a starting point where design inputs and parameters are declared and assumptions established. In this analysis, the design inputs are mainly the flight altitude and the vehicle maximum skin temperature.

All numerical processes are described in a cylindrical coordinate frame of reference,  $x$ ,  $r$  and  $\phi$ , where the  $x$  axis is aligned with the free stream velocity vector, refer to Figures 7 and 8. The inviscid flowfield variables are defined as follows:  $u$ ,  $v$ ,  $p$  and  $\rho$ , where  $\rho$  is the density,  $u$  and  $v$  the cylindrical velocity components in the  $x$  and  $r$  directions respectively, and  $p$  the pressure. In the case of a prescribed axisymmetric shock wave in the form:

$$r_{1,j} = f(x_{1,j}), \quad x_{1,j+1} = x_{1,j} + \delta x \quad (1)$$

along with the appropriate data tabulated in Table 1, the flowfield parameters behind the shock wave are computed based on the numerical analysis methods described in Ref 15 – 22 . Further, the numerical routine yields a set of  $M$  streamlines,  $IS_{i,j}$ , with each streamline consisting of  $N$  nodes. Moreover, in this analysis, the inviscid solution, representing the hypersonic flowfield,  $SL_{inv}$ , is considered a set of  $M$  streamlines defined as  $IS_{i,j}$ , such that,

$$SL_{inv} = IS_{i,k}^{U,L}(x, r, \rho, u, v, p); \quad i \in (1, N), \quad k \in (1, M) \quad (2)$$

The index  $k$  in equation (2) represents the streamline of interest and the index  $i$  represents the coordinates of a given streamline, where the inviscid flowfield properties,  $u$ ,  $v$ ,  $p$  and  $\rho$ , are stored. Refer to Figure 7.

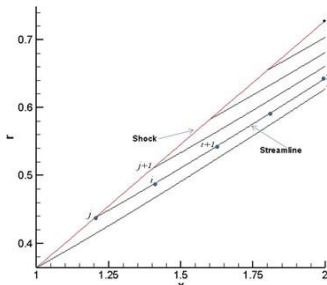


Fig 7. Computational Marching Scheme

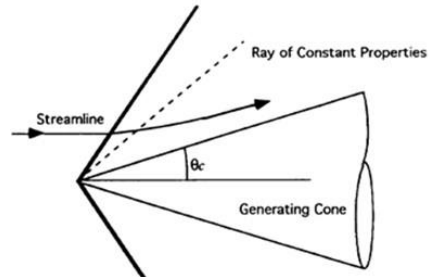
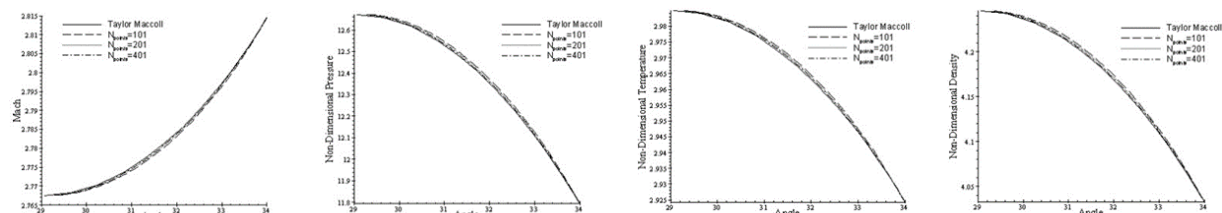


Fig 8. Taylor Maccoll Solution

Inviscid flowfields,  $FF_{inv}$ , obtained from the explicit marching scheme implemented in this analysis were compared to the Taylor-Maccoll analytical solution. The results of comparing the inviscid properties of the two flow fields at a flight velocity of 1.95 km/s and a half cone angle of  $34^0$ , is presented in Figure 9. The Taylor-Maccoll procedure solves the Euler equations in form of spherical coordinates and facilitates the transformation of the system of partial differential equations into a single ordinary differential equation that is easily solved using the Runge-Kutta scheme. Note that the Taylor-Maccoll solution generates the flow properties,  $\rho$ ,  $u$ ,  $v$  and  $p$ , as functions of the angle,  $\theta$ , the angle of measure between the generating cone angle and the shockwave angle, as illustrated in Figure 8.



9a: Mach Distribution

9b: Pressure Distribution

9c: Temp Distribution

9d: Density Distribution

Fig. 9: Comparison of Conical Solutions from the Waverider Code and the Taylor Maccoll Procedure

The solution generated by the marching scheme used in this waverider analysis provides the flow properties,  $\rho$ ,  $u$ ,  $v$  and  $p$ , along the streamlines. After some minor transformation, the solution,  $\rho$ ,  $u$ ,  $v$  and  $p$ , in non-dimensional form obtained from the two procedures are compared and illustrated in Figure 9. Under these flight conditions, a grid independent test was also carried out, in which the number of grids in the  $x$ -direction was increased from 101 to 201

and next to 401. During this test no significant variations in the solution were observed, as supported by the plots illustrated in Figures 9.

## B. Transforming Inviscid Streamlines to Viscous Streamlines

Using the inviscid properties along the stream lines defined in equation (2), along with the established empirical correlations of evaluating the viscous properties; the local shear stress,  $\tau$ , the local heat flux,  $\dot{q}$ , and the local boundary layer thickness,  $\delta$ , the local surface normal,  $\vec{n}$ , and other viscous related properties of interest to this analysis are computed , (Ref 15, 21, 22). With the viscous properties now defined along the inviscid streamlines, they are now considered viscous streamlines. In this analysis, the viscous streamlines are defined as follows:

$$SL_{vis} = VS_{i,k}^{L,U}(x, r, \delta, \tau, \dot{q}, \vec{n}); \quad i \in (1, N), \quad k \in (1, M) \quad (3)$$

The effects of boundary layer transition on the skin friction coefficient and the shear stress are incorporated in the transformation (Ref 21). The shear stress,  $\tau$ , at each point of the inviscid streamlines identified in equation (3) is evaluated as follows;

$$\tau = \frac{1}{2} \rho_e u_e^2 C_{f,x}; \quad C_{f,x} = \begin{cases} C_{f,x,Lam}; & x \leq x_{Trans,Start} \\ C_{f,x,Turb}; & x_{Trans,Start} \leq x \leq x_{Trans,Stop} \\ C_{f,x,Trans}; & x \geq x_{Trans,Stop} \end{cases} \quad (4)$$

where the transition distances;  $x_{Trans, Start}$ , and  $x_{Trans, Stop}$ , are defined later in this paper. In addition, the skin friction coefficient,  $C_f$ , distribution along the streamlines is evaluated using the Reference Temperature Method in a manner similar to the approach implemented in Ref. 21. Similarly, the local Stanton number,  $St$ , the local boundary layer height,  $\delta$ , and the local heat flux,  $\dot{q}$ , are computed, see Ref. 21.

It is of interest to note that the viscous quantities of interest to this analysis are computed in three regions; namely, the laminar, turbulent and transition regions, as described by equation (4). Moreover, the transition point,  $x_{Trans, Start}$ , is assumed to exist at the location defined the transition Reynolds number,  $Re_{Trans}$ , as follows:

$$\log(Re_{Trans}) = 6.421 \exp(1.209 \times 10^{-4} M^{2.641}) \quad (5)$$

and the end of transition,  $x_{Trans, Stop}$ , is determined using the Reynolds number relationship developed by Chen and Thyson and implemented in the form suggested by Cebeci,

$$Re_{ETrans} = C Re_{Trans}^{2/3} + Re_{Trans}; \quad C = 60 + 4.86M^{1.92} \quad (6)$$

where  $M$  is the local Mach number on an inviscid streamline. The transition viscous properties are computed through the use of the intermittency factor,  $\zeta_{tr}$ , and the local skin friction coefficient and Stanton Number,  $C_f$  and  $St$ . In this paper, these quantities are computed as a sum of two fractions relative to their laminar and turbulent values, such that,

$$\chi = \zeta_{Trans} \chi_{Lam} + (1 - \zeta_{Trans}) \chi_{Turb}; \quad \chi_{Turb} = \begin{cases} C_f \\ St \end{cases} \quad (7)$$

Equation (7) is applicable in the cases of both local skin friction and local heat flux. The intermittency factor,  $\zeta_{tr}$ , is evaluated through the use of Cebeci's correlation,

$$\zeta_{Trans} = 1 - \exp\left[-\left(\frac{G}{u}\right)(x - x_{Trans})^2\right] \quad (8)$$

where the beginning and end of transition,  $x_{Trans, Start}$ , and  $x_{Trans, Stop}$ , and the variable,  $G$ , are defined as follows:

$$x_{Trans} = \frac{\mu Re_{Trans}}{\rho u}; \quad x_{Trans, Stop} = \frac{\mu Re_{Trans}}{\rho u}; \quad G = \left( \frac{3}{C^2} \right) \left( \frac{\rho}{\mu} \right)^2 u^3 Re_{Trans}^{-1.34} \quad (9)$$

For the analysis conducted in this paper, the viscous engineering correlations used in transforming the inviscid streamlines into their viscous counterparts are mainly based on the theory of compressible flow over flat plates. Since these engineering correlations are fairly well established, the validation tests conducted herein were designed to demonstrate that these relationships were properly implemented. The viscous properties generated during streamline transformation were compared to the experimental findings of Neal. The data obtained from these test were prepared in the form of the local skin friction coefficient versus the local Reynolds number, and the local heat flux versus the local Reynolds number, and plotted in Figures 10 and 11.

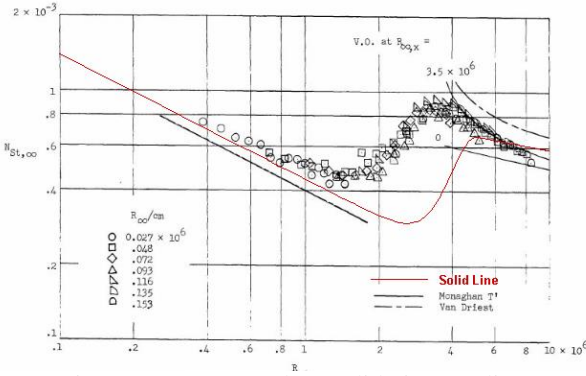


Fig 10. Stanton Number Validation Studies

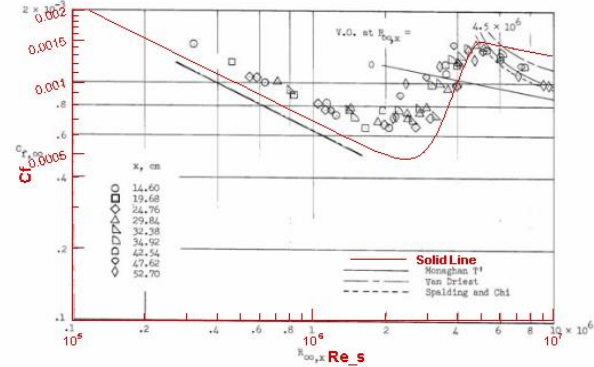


Fig 11. Skin Friction Coefficient Validation Studies

In both tests, the viscous results generated by the model used in this waverider analysis are overlaid in red onto the graphs extracted from Neal. These plots show that the behavior of laminar and turbulent computations are in good agreement with their experimental findings. It is observed that in the cases of both the laminar and turbulent flows, the waverider model delivers agreements that are in line with the Monaghan's, Van Driest and Spalding-Chi's models. However, with respect to the Stanton Numbers, the waverider model somewhat overshoots the transition regions when compared to Neal's experimental data. At this time, these studies are very optimistic and may serve the hypersonic design community well, as flight data show that transition occurs later in atmospheric conditions when compared to laboratory environments.

### C. Waverider Construction and Analysis

In summarizing the achievements made, the flowfield has been constructed, the inviscid streamlines extracted and the viscous streamlines developed. Three-dimensional waverider configuration can be now be extracted from these viscous streamlines. The process of constructing waverider configurations is best described through the use of the two illustrations presented in Figures 12 and 13. Generally speaking, waveriders are 3-D configurations, and therefore, three coordinates are needed to fully define its shape. So far in this analysis, only two coordinates; namely,  $x$  and  $r$ , were obtained. An appropriate set of  $\phi$ -coordinates is therefore needed. For the purposes of this paper, the set of  $\phi$ -coordinates that will completely define a given waverider; is termed the 'shape-angle' function.

Recall, in the case of an axisymmetric flowfield, the shape of the waverider is defined in cylindrical coordinates,  $x$ ,  $r$ , and  $\phi$ , where the  $x$ -axis is along the waverider's length. In order to make the shape three-dimensional, the  $r$  coordinates need to be rotated by the angle  $\phi$ . The shape angle,  $\phi$  is best defined by choosing a base plane curve in which  $\phi = \phi(r)$  for  $x = L$ , refer to Figure 12. With the set of shape angles fully defined, a 3-D waverider configuration can be constructed, see Figure 13. In this analysis, a given waverider configuration is represented by the expression,

$$W = W_{i,j,k}^{U,L}(x, y, z; p, \tau); i \in (1, N), j \in (1, M), k \in (1, M) \quad (10)$$

where the subscripts, U and L, represent the upper and lower surfaces, and the indices,  $i$ ,  $j$ , and  $k$ , represent the number of coordinates in the respective axes that completely describe the waverider geometry.

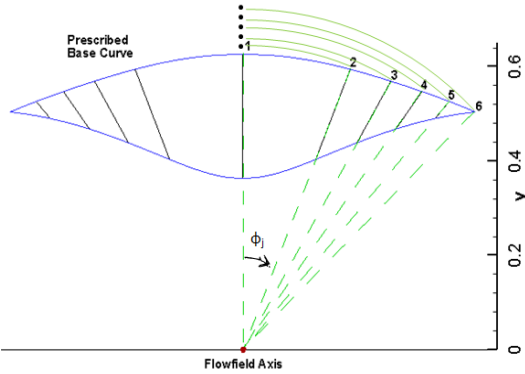


Fig. 12. Waverider Shape Function

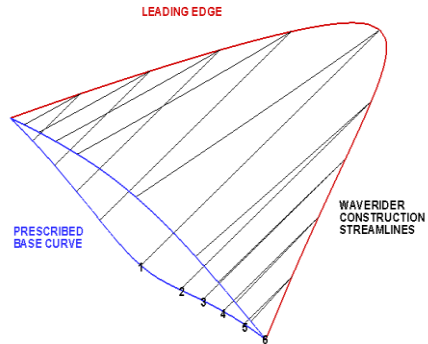


Fig. 13. Waverider from Streamlines

For example, two sets of ‘shape- angle’ functions that were defined through the use of the ‘shape- angle’ illustration presented in Figure 16 can be expressed as follows:

$$\phi_j = \begin{cases} \arccos\left(r_{N+1,1}^{upper} / r_{N+1,j}^{upper}\right) & \text{Flat Top Waverider} \\ \arccos\left(r_{N+1,1}^{lower} / r_{N+1,j}^{lower}\right) & \text{Flat Bottom Waverider} \end{cases} \quad (10)$$

The shape-angle functions above were derived to perfectly describe either a flat top or a flat bottom waverider. Refer to Figures 14 and 15. In a similar manner, other waverider configurations composing of desired features can also be derived. However, at this point only waveriders with sharp leading edges were described, efforts to introduce bluntness are described in the next section.

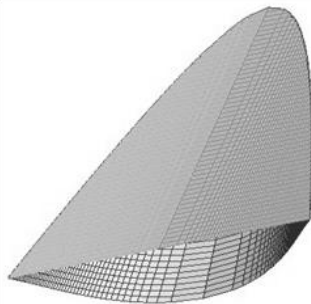


Fig. 14: Flat top waverider

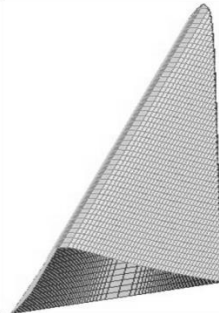
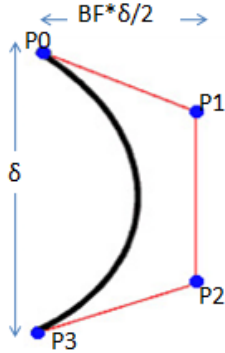


Fig. 15: Flat bottom waverider

#### D. Reshaping the Waverider Leading Edge with Bluntness

The waverider design concept described above inherently generates configurations with sharp leading edges, which poses a nightmare to designers because sharp leading edges are exposed to extremely small stagnation regions and unmanageably large thermal loads. To combat this effect, waveriders with the potential for practical application must incorporate a reasonable degree of bluntness, but care must also be taken to avoid flow spillage from the lower to the upper surface. In principle, the blunting of the leading edge is conducted in the manner illustrated in Figure 20. The concept used in the evaluation of the viscous properties along the blunted surface is illustrated in Figure 21 and described below.



**Fig. 16:** Illustration of blunting waveriders

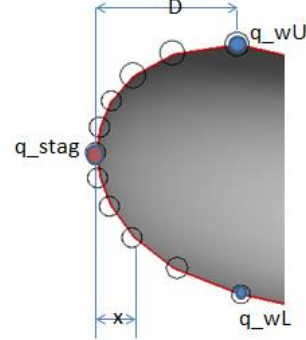


**Fig. 17:** Leading edge heat flux evaluation

First, the upper surface is separated from the lower in the  $y$ -direction by twice the desired blunt radius, such that,

$$WR^U(y) = WR^U(y) + 2R_{\text{BluntRadius}} \quad (11)$$

Next, the separated surfaces are reconnected with Bezier curves, which form the basis of the leading edge curves. A Bezier curve is defined by the following expression,

$$F_{BC} = (1-t)^3 P_0 + 3t(t-1)^2 P_1 + 3t^2(1-t)P_2 + t^3 P_3; \quad 0 \leq t \leq 1 \quad (12)$$

The four required control points;  $P_0$ ,  $P_1$ ,  $P_2$  and  $P_3$ , that defines a given Bezier curve,  $F_{BC}$ , are determined using the slopes and leading edge points of the upper and lower surfaces as illustrated in Figure 20. In this design approach, a blunt factor,  $BF$ , is introduced to control the distance at which the curve extends from the original configuration, thereby controlling the degree of blunting.

The pressure is determined at each point on the blunted surface by using the modified Newtonian relations in the form,

$$P_{i,j} = q_\infty C_{p,i,j} \quad (13)$$

with the aid of the following two expressions:

$$C_{p,i,j} = C_{p,\max} \frac{|V_\infty \cdot \hat{n}_{i,j}|^2}{V_\infty^2}; \quad C_{p,\max} = \frac{2}{\gamma M_\infty^2} \left[ \left( \frac{(\gamma+1)^2 M_\infty^2}{4\gamma M_\infty^2 - 2(\gamma-1)} \right)^{\frac{\gamma}{\gamma-1}} \left( \frac{1-\gamma+2\gamma M_\infty^2}{\gamma+1} \right) - 1 \right]$$

In addition, the local unit normal,  $\hat{n}_{i,j}$ , is evaluated with the use of the expression,

$$\hat{n}_{i,j} = \frac{(Point_{i+1,j} - Point_{i-1,j}) \times (Point_{i,j-1} - Point_{i,j+1})}{|(Point_{i+1,j} - Point_{i-1,j}) \times (Point_{i,j-1} - Point_{i,j+1})|} \quad (14)$$

In a similar manner, the heat flux distribution along the blunted surface is determined using the stagnation heating relationship for hypersonic viscous flows. The stagnation heat flux is considered at the mid of the blunt surface, where it is assumed that  $t = 0.5$  along a given Bezier curve. In this analysis, the stagnation heat flux is determined by using Fay-Riddell relationship [Ref. 27],

$$\dot{q}_0 = 0.537a \Pr_w^{-0.6} \left( 1 + \left( \frac{Dx}{Dz} \right)^{0.5} \right)^{0.5} \left( \frac{du_e}{dx} \right)_{x=0}^{0.5} \left( 1 + (\text{Le}^d - 1) \left( \frac{h_{De} - h_{Dw}}{h_e - h_w} \right) \right) (h_r - h_w) \quad (15)$$

where the auxiliary symbols are defined as follows:

$$\left( \frac{du_e}{dx} \right)_{x=0} = \frac{2}{D_x} \sqrt{\frac{2(P_t - P_e)}{\rho_t}}; \quad a = (\rho_t \mu_t)^{0.4} (\rho_w \mu_w)^{0.1} \quad (16)$$

The variables  $D_x$  and  $D_z$  are the principal diameters, such that,  $D_x < D_z$ , and the other parameters are chosen as follows:  $Le = 1.0$  and  $d = 0.52$ , since disassociation is not considered. The boundary layer edge pressure is considered equivalent to the wall pressure. The local heating along the blunt surface was estimated via interpolation between the stagnation and upper and lower heating points, respectively. Refer to Figure 21. The interpolation procedure used the Fay-Riddell equation with the local edge properties approximated using the following interpolation expression,

$$\chi_{LE} = \frac{x^p}{D^p} \chi_{wL,wU} + \left( 1.0 - \frac{x^p}{D^p} \right) \chi_{stag,e} \quad (17)$$

Similarly, the skin friction coefficient across the blunted surface is also approximated via interpolation between the stagnation point and the upper and lower surfaces. The skin friction coefficient at the stagnation point is zero and increases to its maximum value at the point where the lower and upper surfaces meet the blunted surface. It is assumed to increase in a trend similar to the  $y$ -component of the normal vector along the blunt surface. Therefore, in this case, the interpolation relationship is not necessarily linear, but rather, expressed with the relationship,

$$C_{f_{Pt}} = \frac{ny_{Pt}x^p}{ny_{Pt}} C_{f_{L,U}} \quad (18)$$

In this study, twenty-five waverider configurations were created with blunted leading edges and studied. Each waverider was created from the same axisymmetric flowfield. However, each waverider was curved based on its own unique set of shape angles,  $\phi$ . For illustrative purposes, samples of two waveriders; a ‘Bowcutt-type viscous optimized’ waverider and a ‘Batwing-type viscous optimized’ waverider, were evaluated for high altitude applications and presented in Figures 18 and 19.

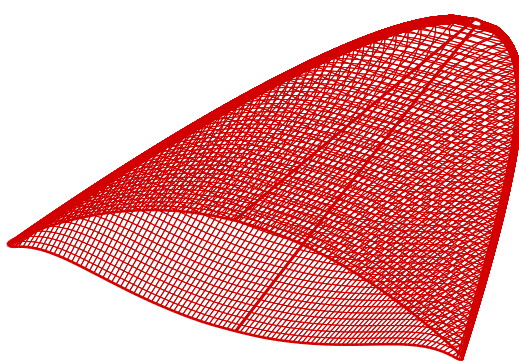


**Fig. 18:** Bowcutt-type viscous optimized’ waverider

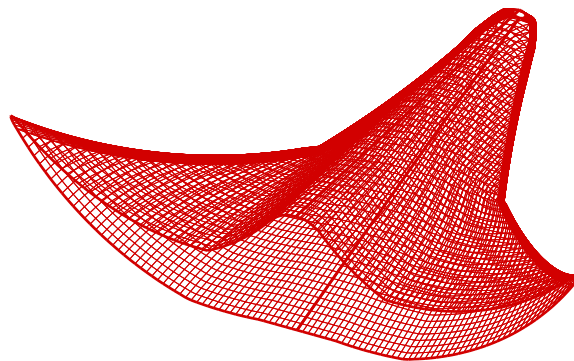


**Fig. 19:** Batwing-type viscous optimized’ waverider

#### E. ‘Waverider derived’ Hypersonic Vehicles

Using the design approach developed herein, generalized stream surfaces may be carved from prescribed inviscid flow fields and used as auxiliary surfaces in the design of hypersonic vehicle and scramjet engine components. In general, a generic stream-surface is not restricted to the rules of a ‘waverider stream-surface’ and may be formed by any set of neighboring solid-lines. Auxiliary stream-surfaces can be formed in ways similar to that of the waverider surfaces, with a base curve definition or a generalized ‘shape-angle’ function. This freedom in the design procedure allows for the creation of a completely streamlined hypersonic vehicle with integrated components. Examples of possible designs are presented in Figures 20 and 21. In Figure 21 an auxiliary stream-surface, serves as an engine

component, and demonstrates potential design process for constructing an entire vehicle using this waverider design technique. Figure 20 demonstrates the use of many surfaces to create a ‘complete’ hypersonic vehicle.

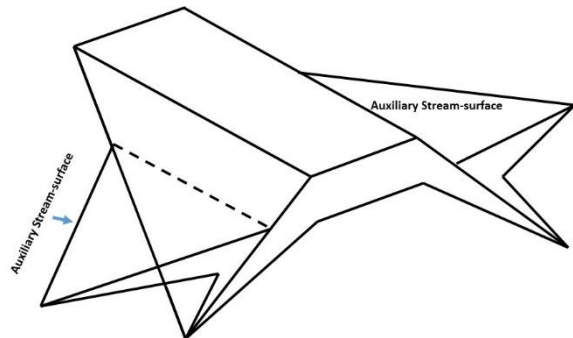


Fig.20: Waverider with control surfaces.

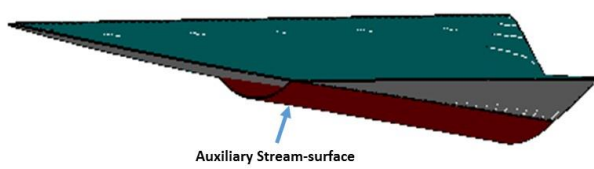


Fig.21: Waverider with ducted stream-surface.

### III. Independent Evaluation of Waverider Design Methodology

#### A. Comparative Studies with CFD

In an effort to further validate the waverider design methodology; examine the integrity of its analysis methods; and measure the degree of success of its grid generation procedure, an extensive and independent CFD analysis was conducted. Euler, laminar and turbulent case studies were conducted. The computational grids were created to best model, both, the fluid physics over the waverider configurations at hypersonic speeds, and the unique geometric features of the ‘streamlined body’ and ‘blunted leading edges’ of each waverider. Also used in these studies were the Air Vehicles Unstructured Solver (AVUS) CFD aerodynamic analysis tool, and the flow field visualization tool, Tecplot<sup>TM</sup>. AVUS is a finite volume unstructured-grid Euler and Navier-Stokes solver developed at Air Force Research Laboratory. Its algorithm is cell-centered, first-order accurate in space and time and based on exact Riemann solver of Godunov<sup>28</sup>. Tecplot<sup>TM</sup> is a commercially available tool, commonly used in the CFD industry.

The Mach number and the other design inputs for the case study was guided by the requirements of the hypersonic glide corridor and to some extent, the capabilities of Navier-Stokes solvers. The pressure and temperature were hardwired. The conditions set for the test case are as follows:

**Table 2 Conditions for chosen case study**

| R <sub>Bluntness</sub> (%) | M <sub>inf</sub> | P <sub>inf</sub> (N/m <sup>2</sup> ) | T <sub>inf</sub> (K) | T <sub>Wall</sub> /T <sub>inf</sub> |
|----------------------------|------------------|--------------------------------------|----------------------|-------------------------------------|
| <b>0.25</b>                | <b>6.0</b>       | <b>290.0</b>                         | <b>290.0</b>         | <b>Adiabatic</b>                    |

The flow was initialized as free stream. The boundary condition were prescribed as follows; symmetry plane was set as a slip wall, waverider surface as no slip walls and the remaining bounds of the volume mesh as a modified Riemann invariant far field. The focuses for comparisons were shock shape, shock location, flow field, surface pressure and overall aerodynamic performance.

#### B. Comparative Euler Flow-field Analysis

In the Euler study, the waverider surface was consider as a slip wall. In this case, the behavior of the flow field within the neighborhood of the waverider is of upmost interest. Figure 22 shows the overall flow field in terms of pressure. It clearly illustrates an axis-symmetric like flow field about the lower surface of the waverider. It is important to observe the shape of the shock that emanates from the leading edge. Figure 23 gives a closer look where the Euler results are compared at the base plane to the flow field used to construct the waverider. The comparison show the shape and location of the shock are in close agreement. In addition, the pressure distribution throughout the flow field closely agrees as well with small discrepancies that can be explained. For example, the construction flow field was used to derive an ideal waverider whereas the CFD study was conducted on a blunted waverider. Therefore, the offset of the shock is due to the small addition of blunting which causes the shock to standoff from its ideal location.

Also due to blunting, and as expected, there is some leakage of flow and thus pressure variation around the leading edge shown in Figure 23. However, the leakage does not greatly influence the pressure distribution across the upper surface, which sees uniform pressure close to the free stream value, thus yielding the expected designed characteristics. In addition, the pressure along the lower surface is dictated by the post-shock flow field. These results strongly confirm the legitimacy of the waverider inverse design methodology.

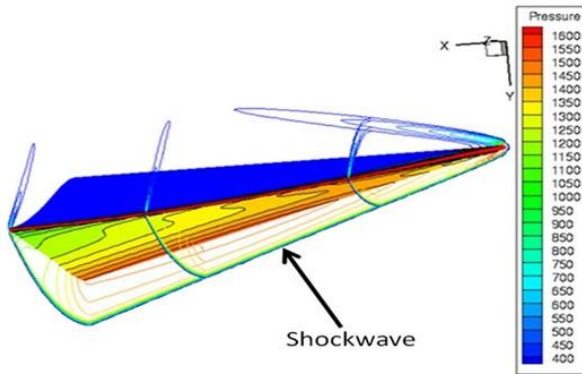


Fig. 22: Waverider Euler Pressure Evaluation

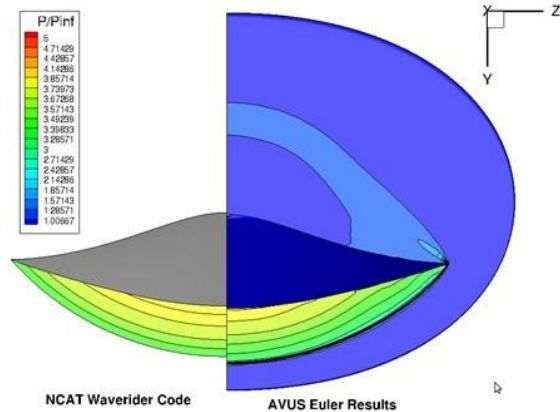


Fig 23: Waverider Euler base pressure comparison

Figures 24 and 25 reiterates the comparison of the flow fields at the symmetry plane. Again, the higher pressures in the nose region of the Euler study display the effects of the leading edge and blunting. The induced pressure rise towards the leading edge due to blunting deteriorates downstream yielding a pressure distribution similar to the flow field that does not account for blunting.

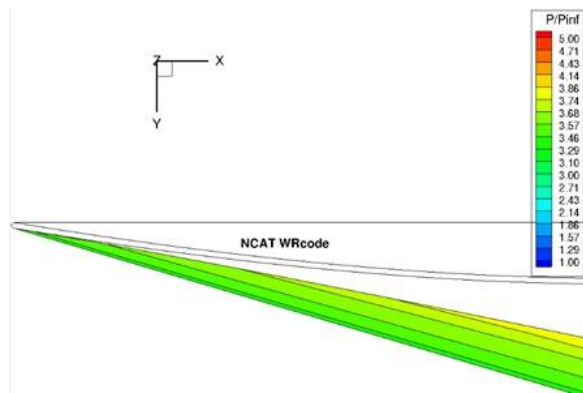


Fig. 24: Semi analytical flow field at symmetry plane

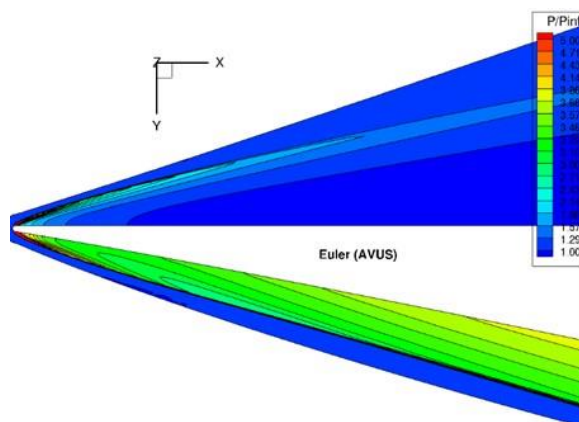


Fig. 25: Comparison of pressure ratio at symmetry plane

Another technical feature of interest to design engineers and subject for comparison are the streamlines location and behavior. Recall, the upper and lower surfaces were formed by tracing streamlines. Figure 26 shows the streamlines along the surface resulting from the Euler study of the blunted waverider (colored in black) overlaid onto the streamline mesh that formed the ideal surfaces (colored in red). The streamlines of the Euler study clearly depict the stagnation line in the mid-region of the blunt surface where stagnation was assumed. Figures 27 and 28 show the Euler study streamlines overlaid onto upper and lower surface streamlines respectively. For both cases, the streamlines are in close agreement close to the leading edge but veer off towards the tip downstream. This may be due to the blunt surface design, which influences the flow towards the tip. The influence is stronger on the lower surface than the upper surface. However, it is important to acknowledge the streamlines that emanate from the nose region want to

deviate towards the root of the waverider. It is not clear as to why this may be the case. One suspicion is there may be some deviation in the geometry close to the nose region that was not detected during the visual inspection of the mesh. Even with the disagreements between the particular streamlines, the general flow field was recovered as presented in the pressure contours. Therefore, minor discrepancies that may be present in the geometry do not greatly disturb the overall flow field.

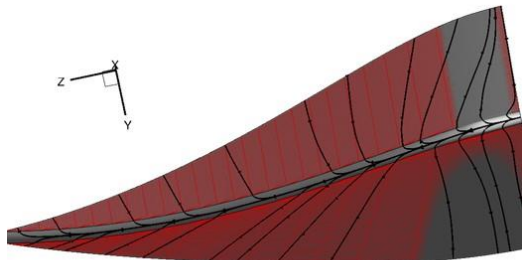


Fig. 26: Streamlines emanating from blunt surface

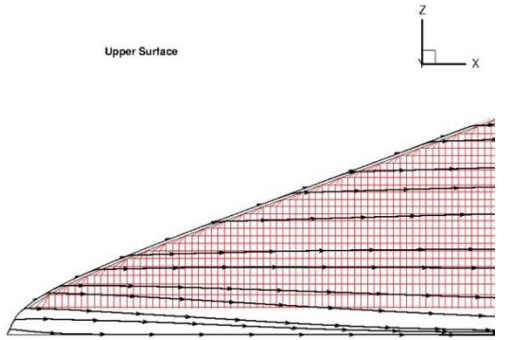


Fig. 27: Streamline comparison on upper surface

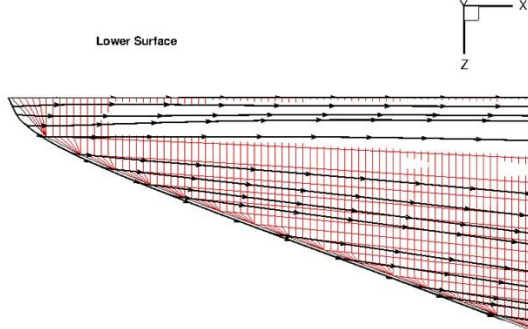


Fig. 28: Streamline comparison on lower surface

### C. Comparative Viscous Flow-field Analysis

In efforts to validate the newly created waverider analysis methods, both laminar and turbulent CFD studies were conducted, again using the independent AVUS tool, while the local surface properties were compared. During this case study, the turbulence model selected was the Spalart-Allmaras model. The results of the laminar and turbulent flow fields were prepared in identical plots and displayed in Figures 29 – 32 for ‘side-by-side’ comparison. In this study, the effects of blunting, viscosity and turbulence were observed. The turbulent and laminar Mach contour comparison at the base plane, presented in Figure 29, shows the existence of a boundary layer for both cases as expected. Furthermore, the turbulent boundary layer is thicker at the base cross-section. Thus, the shock is further detached from the body as assumed in the automated grid generation process.

The pressure contour comparison, presented by Figure 30, shows the effects of a thicker boundary layer within the flow field. Boundary layer theory concludes that pressure along the normal from the surface does not change within the boundary layer. This is also captured in the pressure contour line results shown in Figures 31 and 32. However, beyond the boundary layer the flow fields are quite comparable to the flow field from which the waverider is constructed. It is also worthy to note that the flow field induced by and around the blunting is further influenced by the addition of viscous and turbulent effects. Figure 30 highlights the enhancement of the viscous-blunting leading edge effect due to turbulence. Whether this can be attributed to the actual existence of turbulence or merely an artifact of the turbulence model has yet to be determined or speculated.

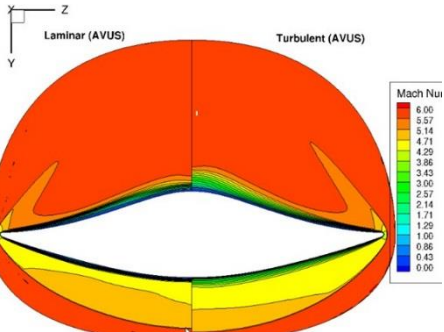


Fig. 29: Laminar vs. turbulent base plane Mach

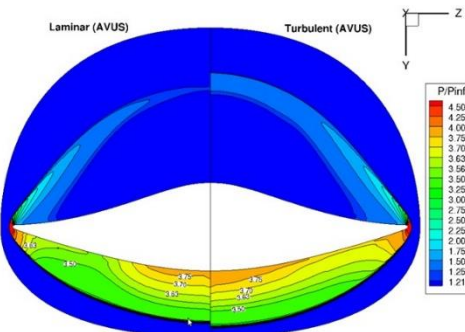


Fig. 30: Laminar vs turbulent base pressure ratio

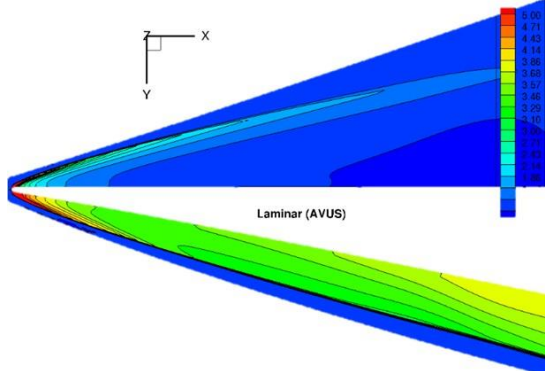


Fig. 31: Laminar pressure at symmetry plane

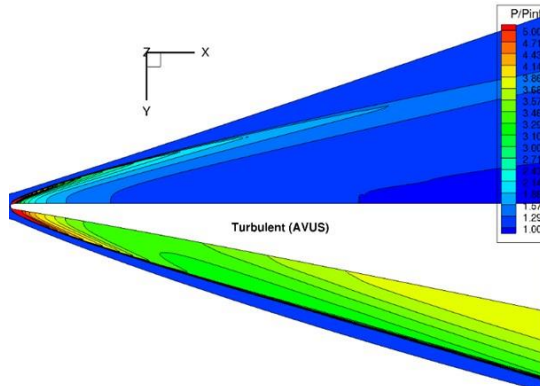


Fig. 32: Turbulent pressure ratio at symmetry plane

The results of a second viscous CFD study demonstrated that the far-field pressure distribution around the waverider under design conditions was recovered. As illustrated in Figure 33 and Figure 34, the waverider appears to be riding its own shock wave. A relatively weak blunt shock wave with a small standoff distance is captured along the leading edge of the vehicle as seen in the Euler study. Again, the shape of the shock resembles the prescribed design shock. A closer look of the pressure flow field is illustrated in Figure 34. There it can be seen that not only is the flow field on the under belly of the waverider uniformly conical, but at cross-sections of one-thirds, two-thirds and at the base of the vehicle show remarkable similarity of that reminiscent of a conical flow field as well.

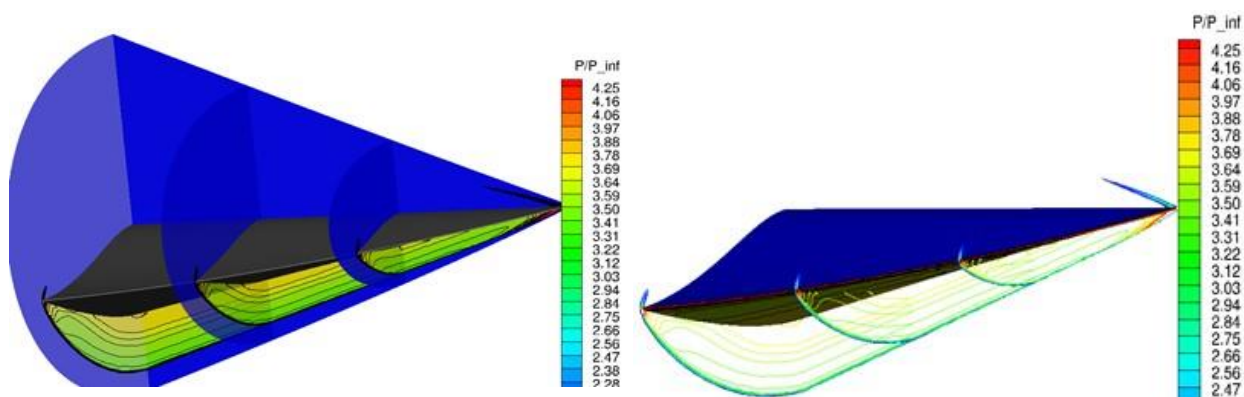


Fig. 33: Pressure field results

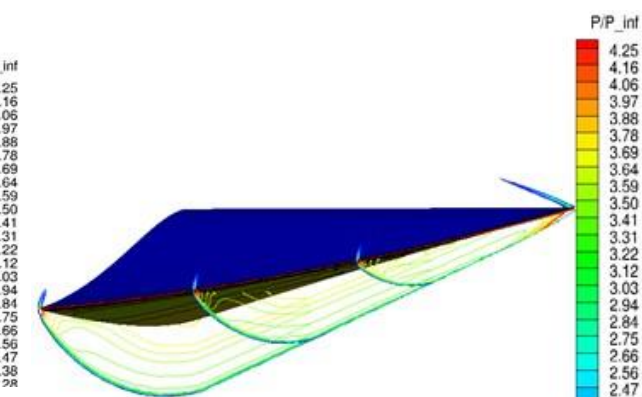


Fig. 34: Shock with pressure results

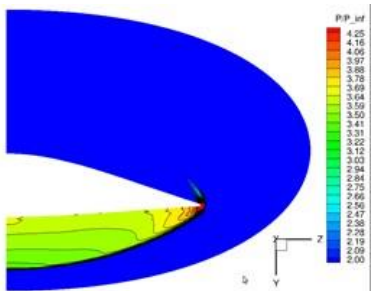


Fig. 35a: Quarter Chord Base Plane

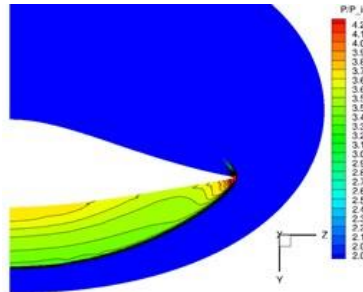


Fig. 35a: Semi-Chord Base Plane

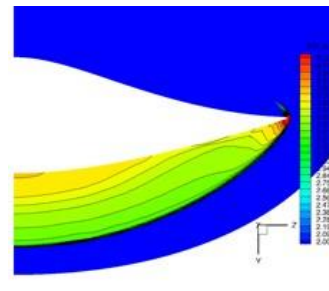


Fig. 35a: Base Plane

Fig. 35: Pressure distribution at cross-sections of one-thirds, two-thirds and base plane

#### D. Viscous Flow-field Analysis in Axisymmetric Planes

Figure 36 presents the Mach contours at the symmetry plane with streamlines for the laminar flow field. The streamlines indicate the validity of the design methodology by displaying the flow traveling parallel to the upper surface and being processed by the shock at the lower surface.

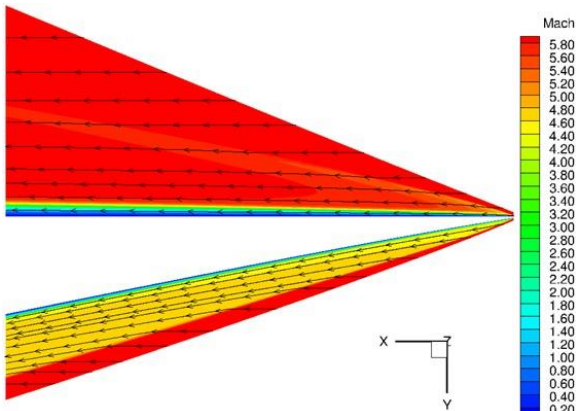


Fig.36: Streamline distribution and boundary layer thickness recovery

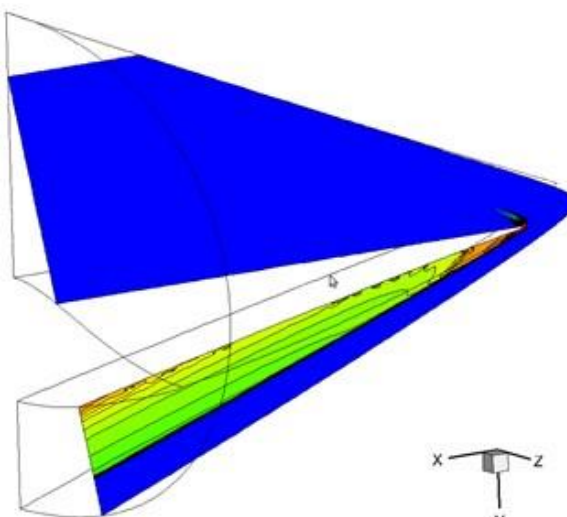


Fig. 37: Azimuthal plane (20° inclined)

Additionally presented in Figure 37 is an azimuthal plane of the pressure distribution contour. Figure 37 illustrates the pressure distribution in an azimuthal plane approximately 20° relative to the symmetric plane. Each plane illustrates that the bulk of the flow field remain conical, except for regions close to the leading edge which show the induced pressure region. Reviewing Figures 36 and 37, one can observe that the induced pressure region covers a set area along the leading edge. Thereby, showing a relatively larger effect within the smaller cross-sections. Again, evidence of the recovery of a conical flow field is clearly visible. However, the influence of the leading edge is visible as well. Nonetheless, CFD studies have reaffirmed the capability of the design methodology to create waveriders by reproducing a similar flow field from which the waverider is derived

#### E. Waverider Surface Analysis

The viscous effects displayed in the flow field translate to the pressure distribution on the surface. Recall the inviscid surface pressure is determined by the constructed streamlines and the viscous surface pressure incorporates the viscous interaction parameter. Figures 38 and 39 presents the comparison between the inviscid surface pressure and the viscous surface pressure determined, for the lower and upper surfaces, respectively. As expected, there is a

higher-pressure region in the empirical viscous result along the leading edge as well as an overall higher pressure across the entire surface. This holds true for both the lower and upper surfaces. It is interesting to observe that the viscous pressure distribution on the lower surface no longer alludes to a conical flow except for the region that is downstream towards the centerline. However, the pressure distribution on the upper surface hints at a conical flow surrounding the surface. Recall, the size and presence of the blunt surface has not been taken into account. Therefore, the differences between the surface pressures are strictly driven by viscous interaction with the leading edge according to the model employed.

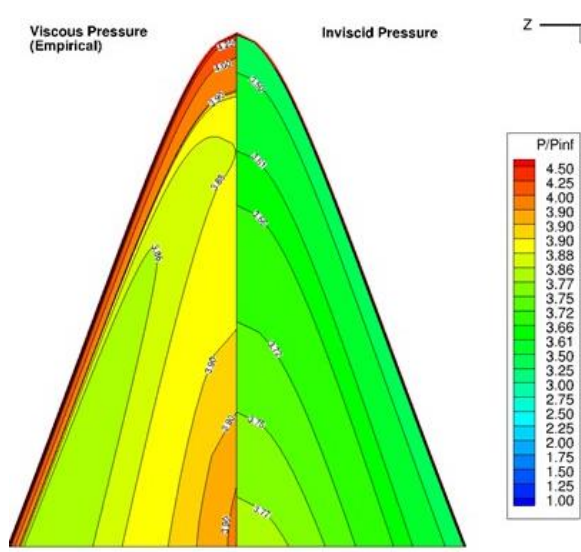


Fig. 38: Inviscid vs viscous lower surface pressures

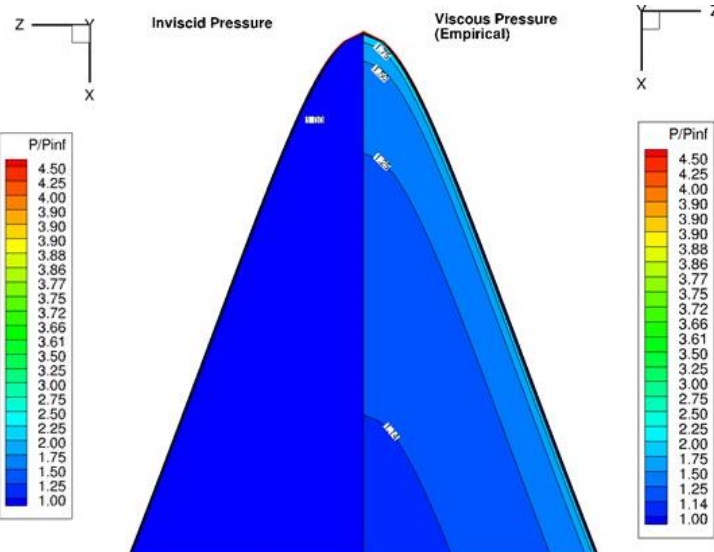


Fig. 39: Inviscid vs viscous upper surface pressures

For the purpose of curiosity, the CFD viscous (turbulent) pressure distribution was compared to the CFD inviscid (Euler) for the upper surface, as presented in Figures 40 and 41. Notice blunting does not induce an increase in pressure across the entire surface like the viscous model. The turbulent results show the combination of influences from blunting, viscosity and turbulence. A small region which is downstream towards the root is unaffected by the leading edge effects. This is contrary to the viscous model used, which suggests that pressure across the entire surface would be higher relative to an inviscid study. This contradiction is further illustrated in Figures 40 and 41 with the comparison of the viscous model results and the turbulent CFD results for the upper and lower surfaces, respectively. Here all but the leading edge seem to disagree. However, the added blunting effect present in the CFD yield disagreement in the nose region.

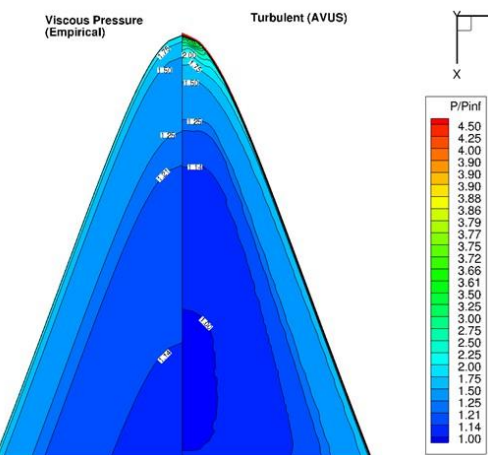


Fig. 40: Viscous surface pressures

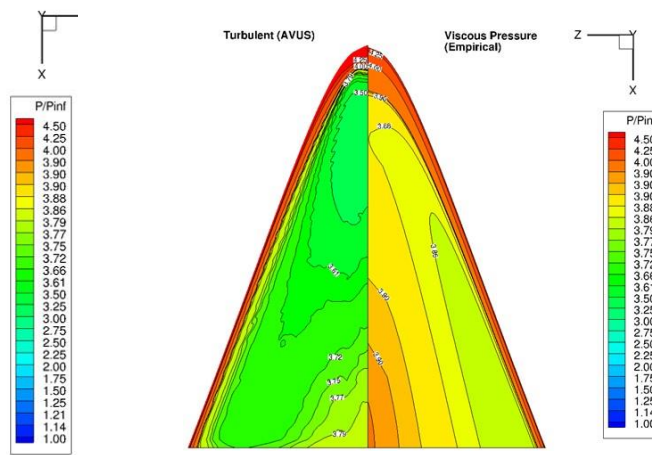


Fig. 41: Viscous lower surface pressures

The lower surface comparison, Figure 42 shows more of a disagreement with contour lines and values. The viscous pressure model showed very poor agreement with CFD. Figure 43 presents the comparison of the inviscid (streamline) model, denoted as NCAT WRcode, with the CFD turbulent model. Strangely, the pressure from the pure streamline matches closer to the turbulent solution downstream towards the root. Also the middle of the surface shows a low pressure region that is less than any pressure along the inviscid surface. This data seems to suggest that there is an expansion being experienced slightly downstream from the leading edge. In addition, the intensity of the expansion would possibly be governed by the change in geometry immediately downstream of the leading edge.

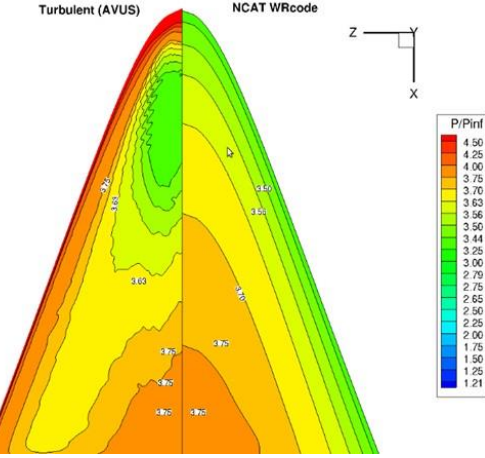


Fig. 42: Turbulent lower surface pressures

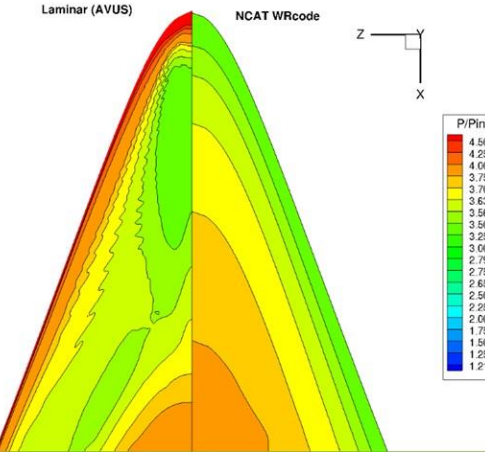
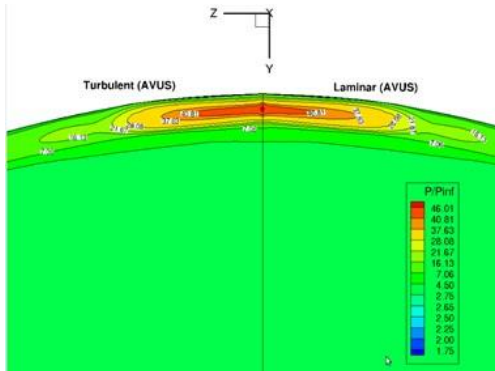


Fig. 43: Laminar lower surface pressures

For the nose region of the blunt surface, Figure 44 shows that the laminar and turbulent results are in good agreement. Similarly, as presented in Figure 45, the modified Newtonian theory does not only agree well with experimental data but also the CFD analysis. This reassures the use of modified Newtonian theory for the blunt surface.



NCAT WRcode, the waverider design space can be formed and used to derive configurations which satisfy the much needed technical requirements of highly integrated fore-bodies, engine and nozzle after-bodies suggested by Kuchemann. The ‘waverider based design’ concept is flexible enough to allow for the creation of a hypersonic vehicle through the assembly of stream surfaces from either a single or multiple independent hypersonic flow fields. As part of this effort, a method for blunting the inherently sharp leading edges of idealized waveriders was formulated using Bezier curves and executed to deliver waveriders with an acceptable degree of sharpness. The design approach adopted in this paper is parametric; for example, leading edge shapes and ‘viscous-transformed stream’ surfaces can be manipulated to result in waverider configurations for practical designs. In addition, an aerodynamic performance analysis method was created and validated.

Currently, the aerodynamic performance analysis method is capable of determining the local pressure, the convective heat flux, and the skin friction coefficient. In addition, the analysis method is equipped with the capability of evaluating the viscous stresses on blunt surfaces by either using a strategic implementation of Fay-Riddell model or the modified Newtonian theory. Each step of the design and analysis process, which includes post-shock flow field generation, viscous design space, ideal waverider formation, blunting, and full analysis, were validated. The flow field generating scheme, Ferguson’s Ref. 9, semi analytical solution to the Euler equations, agreed well with the analytical Taylor-Maccoll solution. It was also validated that the empirical compressible flat plate relations with a transition region were implemented properly. However, it is still unclear whether this technique is appropriate to apply to any generic streamline even though it is valid. The process for the analysis of the generic blunt surface has also been validated via comparison to experimental data. The method for integrating the local surface information to determine its aerodynamic performance was discussed and compared to CFD studies. The determined lift compared well with independent analysis but total drag failed to agree with CFD. CFD analyses were not only used to verify the predictive capability of the WRcode, but also to validate the configuration modification methods implemented in the code. After observing the results of a large number of case studies, the inverse design philosophy of the waverider concept with configuration modification methods incorporated was successfully validated. The coupling of design and proper analysis efforts can expedite the design process to meet the demand of quick design to flight turn around by minimizing the conceptual design phase. It is hoped that this suite of design tools are used to meet some of the demands of research in industry and academia for realistic hypersonic research.

## VI. References

- <sup>1</sup>Cheng, H. K., Perspectives on Hypersonic Viscous and Nonequilibrium Flow Research, NASA-CR-190817
- <sup>2</sup>John D. Anderson, Jr., Hypersonic and High Temperature Gas Dynamics, 2nd Ed. From AIAA
- <sup>3</sup>Anderson, John D., Jr. Introduction to Flight, 4th ed. Boston: McGraw-Hill, 2000, pp. 622-626 and 681-707.
- <sup>4</sup>Nonweiler, T. Aerodynamic problems of manned space vehicles. J. Roy Aeronaut Soc, 1959, 63: 521 - 528
- <sup>5</sup>Kuchemann D. The Aerodynamic Design of Aircraft, Oxford: Pergamon Press, 1978. 448 - 510
- <sup>6</sup>Bowcutt, K. F, Anderson, J. D & Capriotti, D. P 1987, ‘Viscous optimized hypersonic waveriders,’ in AIAA 25<sup>th</sup> Aerospace Sciences Meeting, AIAA Paper 87-0272.
- <sup>7</sup>Mangin, B, Benay, R, Chanetz, B & Chpoun, A 2006, ‘Optimization of viscous waveriders derived from axisymmetric power-law blunt body flows’, *Journal of Spacecraft and Rockets*, vol. 43, pp. 990-998.
- <sup>8</sup>Corda, Stephen and Anderson, John D., Jr. Viscous Optimized Waveriders Designed from Axisymmetric Flowfields, AIAA Paper 88-0369, 1988.
- <sup>9</sup>Ferguson, Frederick, Ph. D Dissertation, Department of Aerospace Engineering, University of Maryland, College Park, Maryland, UM-AERO-93-5. 1993.
- <sup>10</sup>Ferguson, Frederick, et al., A Design Method for the Construction of Hypersonic Vehicle Configurations, AIAA 95-6009, Chattanooga, TN, April 3-7, 1995.
- <sup>11</sup>Ferguson, Frederick, and John D. Anderson, Jr., Expanding the Waverider Design Space Using General Supersonic and Hypersonic Generating Flows, AIAA 93-0505, Reno, NV, January 11-14, 1993.
- <sup>12</sup>Jones K.D, & Center K.B, 2002, WaveriderDesign Mehods for Non Conical Shok Geometries, *3rd Theoretical Fluid Mechanical Meeting*, 24-26 June, St. Louis, Missouri.
- <sup>13</sup>Walt Engelund, NASA LARC, 2001, Hypersonic Aerodynamics, <[http://www.dept.aoe.vt.edu/~mason/Mason\\_f/ConfigAeroHyperXsem.pdf](http://www.dept.aoe.vt.edu/~mason/Mason_f/ConfigAeroHyperXsem.pdf)>.
- <sup>14</sup>Scott, J 2004, Hypersonic waverider, Aerospaceweb, viewed 23 December 2011, <<http://www.aerospaceweb.org/design/waverider/examples.shtml>>.

<sup>15</sup>Frederick. Ferguson, Shengyong Zhang and Hydar Apdin, A Design Concept for the Construction of a Complete Hypersonic Vehicle from 2D Flowfields, AIAA/CIRA 13th International Space Planes and Hypersonic Systems and Technologies, AIAA 2005-3363.

<sup>16</sup>Frederick Ferguson, Mookesh Dhanasar, CFD Analysis of an Inlet-Isolator Combination for Dual Mode Scramjet Applications, AIAA-2011-404, 49th AIAA Aerospace Sciences Meeting including the New Horizons Forum and Aerospace Exposition, Orlando, Florida, Jan. 4-7, 2011.

<sup>17</sup>F. Ferguson, and M. Dhanasar, 'A Model for the Design and Analysis of Thrust Optimized Scramjets', AIAA-2009-7337, 16<sup>th</sup> AIAA/DLR/DGLR International Space Planes and Hypersonic Systems and Technologies Conference, Bremen, Germany, Oct., 19-22, 2009.

<sup>18</sup>F. Ferguson, Y. Fiagbe and N. Dasque, 'Design of Optimized 3D Tip-to-tail Scramjet Engines', AIAA-2009-1099, 47<sup>th</sup> American Institute of Aeronautics and Astronautics Aerospace Sciences Meeting and Exhibit, Orlando, FL 2009.

<sup>19</sup>F. Ferguson and M. Dhanasar and I. Blankson, 'Preliminary Design of a Tip-to-Tail Model of a Ram-Scram Jet Engine,' AIAA-2009-714, 47<sup>th</sup> American Institute of Aeronautics and Astronautics Aerospace Sciences Meeting and Exhibit, Orlando, FL 2009.

<sup>20</sup>F. Ferguson, M. Dhanasar, R. Williams, I. Blankson and D. Kankam, 'Supersonic and Hypersonic Air-Breathing Configurations Derived from 2D Flowfields,' AIAA-2008-163, 46<sup>th</sup> American Institute of Aeronautics and Astronautics Aerospace Sciences Meeting and Exhibit, Reno, NV 2008.

<sup>21</sup>Frederick Ferguson, Terry L. Corbett, Jr., Stephen Akwaboa, and Haile Lindsay, "The Development of Waveriders From an Axisymmetric Flowfield", AIAA 2007-847, 45<sup>th</sup> American Institute of Aeronautics and Astronautics Aerospace Sciences Meeting and Exhibit, Reno, NV 2007.

<sup>22</sup>Haile Lindsay, Frederick Ferguson, Stephen Akwaboa and Hydar Apdin, "The Construction of Integrated Hypersonic Vehicles from 2D Flowfields", 42<sup>nd</sup> AIAA/ASME/SAE/ASEE Joint Propulsion Conference & Exhibit (2006).

<sup>23</sup>T. Cebeci and A. M. O. Smith, *Analysis of turbulent boundary layers* vol. 15. New York: Academic Press, 1974.

<sup>24</sup>L. Neal, "A Study of the Pressure, Heat Transfer and Skin Friction on Sharp and Blunt Flat Plates at Mach 6.8," 1966

<sup>25</sup>National Defense Authorization Act for Fiscal Year 2007, Pub. L. No. 109-364, 'Roadmap for the Hypersonics Programs of the Department of Defense Report to Congress', Joint Technology Office on Hypersonics Director, Defense Research & Engineering

<sup>26</sup>H. Hallion, "The Hypersonic Revolution: Case Studies in the History of Hypersonic Technology, Vol. I, From Max Valier to Project PRIME", 1998

<sup>27</sup>W.H. Press, B.P. Flannery, S.A. Teukolsky, and W. T. Vetterling, *Numerical Recipes*. New York: Cambridge University Press, 1986

<sup>28</sup>AFRL CFD Research Branch, "Air Vehicles Unstructured Solver (AVUS): User Manual," ed, 2005